Article

# Hydrophobic Solvation of Gases (CO$_2$, CH$_4$, H$_2$, Noble Gases) in Clay Interlayer Nanopores

Greeshma Gadikota,*,† Baptiste Dazas,† Gernot Rother,‡ Michael C. Cheshire,‡ and Ian C. Bourg*,†

†Department of Civil and Environmental Engineering (CEE) and Princeton Environmental Institute (PEI), Princeton University, Princeton New Jersey 08544, United States
‡Chemical Sciences Division, Oak Ridge National Laboratory, Oak Ridge Tennessee 37831-6110, United States

Ⓢ Supporting Information

ABSTRACT: In the past few years, experimental studies have shown that CO$_2$ is roughly 5 times more soluble in water-saturated clay interlayer water than in bulk liquid water. The fundamental basis of this selectivity remains unknown, as does its relevance to other gases. Here, we use molecular dynamics (MD) simulations and gravimetric adsorption experiments to determine the solubilities of CO$_2$, CH$_4$, H$_2$, and noble gases in clay interlayer water. Our results confirm that clay minerals, despite their well-known hygroscopic nature, have a significant hydrophobic character at the atomistic scale. The affinity of dissolved gases for the clay surface shows significant variations related to the size and shape of the adsorbing molecules and the structuring of interfacial water by clay surfaces. Our results indicate that dissolved gases likely do not behave as inert tracers in fine-grained sedimentary rocks such as shale and mudstone, as routinely assumed in groundwater hydrology studies. Our results have implications for the fundamental science of hydrophobic adsorption, for the use of dissolved gases as tracers of fluid migration in the subsurface, and for low-carbon energy technologies that rely on fine-grained sedimentary rocks, such as carbon capture and storage, nuclear energy, and the transition from coal to natural gas.
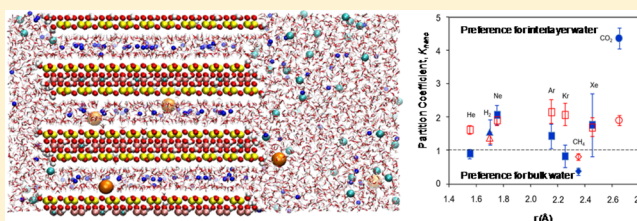
INTRODUCTION

The aqueous geochemistry of dissolved gases in sedimentary rocks is a recurrent topic in groundwater hydrology studies. In particular, it informs noble-gas geochemistry reconstructions of subsurface fluid migration[1,2] and model predictions of the fate and transport of CO$_2$, H$_2$, and CH$_4$ in carbon capture and storage,[3−5] radioactive waste storage,[6,7] and shale gas extraction,[8,9] three technologies with the potential to contribute roughly half of global CO$_2$ abatement efforts over the coming decades.[10,11] Hydrologic studies in these areas invariably assume that dissolved gases behave as inert tracers of fluid migration in water-saturated rocks. The past few years, however, have yielded increasing evidence that aqueous CO$_2$ partitions preferentially into the interlayer nanopores of smectite clay minerals,[5,12−14] the main contributor to the specific surface area and nanoporosity of sedimentary rocks.[15,16] The mechanism of this partitioning remains unknown, as does its relevance to gases other than CO$_2$.

Molecular dynamics (MD) simulations have played an important role in the science of hydrophobic solvation.[17−23] In particular, MD simulations have shown that the free energy of dissolution of gases in bulk liquid water ($\Delta G_{dissolution}$) is the sum of two terms: an entropic contribution associated with the formation of a cavity sufficiently large to accommodate the gas molecule ($\Delta G_{cavity} > 0$) and an enthalpic contribution associated with attractive gas−water interactions ($\Delta G_{affinity} < 0$). The first term is related to the probability P_0 that an empty cavity with a size sufficiently large to accommodate the gas molecule exists at any given location in liquid water. The second term reflects attractive van der Waals and Coulomb interactions between the solute and water molecules.

Molecular dynamics simulations have also been extensively used to probe the interactions of water and solutes with clay surfaces.[24−27] To date, however, few MD simulations have specifically examined the behavior of dissolved gases near hydrated clay surfaces. A significant fraction of these studies have focused on gas coordination and dynamics, not adsorption energetics.[28,29] The few studies that examined the adsorption energetics of dissolved gases[30−32] predicted a strong preference of CO$_2$, but not CH$_4$, for clay interlayer water compared to bulk liquid water, as later confirmed experimentally.[12,13] Molecular dynamics simulation studies, however, have not yet been used to examine the adsorption of gases other than CO$_2$ and CH$_4$ or to elucidate the molecular-scale basis of the predicted selectivity.

Here, we present MD simulations and gravimetric adsorption experiments designed to examine the partitioning of gases of interest in groundwater hydrology (CO$_2$, CH$_4$, H$_2$, noble gases) between bulk liquid water and water-saturated clay interlayer nanopores. Our simulation results are consistent with

experimental data on the solubilities and diffusion coefficients of gases in bulk liquid water.[33−41] Our results reveal that dissolved gases do not generally behave as inert tracers in the presence of clay minerals. Instead, we find that clay surfaces have a significant hydrophobic character at the atomistic scale, as previously noted in the context of cation-exchange selectivity.[42,43] This hydrophobic character is modulated by the presence of exchangeable cations and by the templating of interfacial water by the clay surface. Our results have broader relevance to the adsorption of hydrophobic solutes (including organic molecules)[44] at clay−water interfaces, for example, during sedimentary rock diagenesis,[45] soil formation,[46] and contaminant migration in the subsurface.[47]

■ METHODOLOGY

Molecular Dynamics Simulations. MD simulations were carried out to examine the partitioning of dissolved gases between clay interlayer water and bulk liquid water. The simulated system is almost identical to that used by Tournassat et al.[48] Briefly, the setup consists of a stack of smectite clay layers with 6-Å-wide interlayer nanopores (two-layer hydrate) in contact with a mesopore (Figure 1). Sodium montmor-
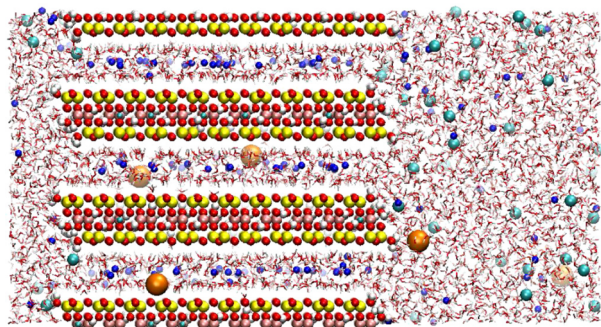

Figure 1. Snapshot of the simulation cell containing three sodium montmorillonite particles (two-layer hydrate) with interlayer nano-pores in contact with a mesopore (0.6 M NaCl solution). Water molecules are shown as red and white sticks; Na and Cl ions are shown as dark and light blue spheres, respectively; and Ar atoms are shown as large orange spheres.

illonite was chosen because nearly half of the sedimentary rock mass consists of smectite or illite (often occurring as interstratified smectite−illite layers) and the specific surface area of smectite is much higher because of its swelling ability. The two-layer hydrate was chosen because it is the major hydration state of smectite in sediments and sedimentary rocks at depths shallower than ∼2 km.[49,50] The simulated smectite structure is a cis-vacant montmorillonite,[51] the most widely studied type of smectite clay mineral. Clay edges were cleaved stoichiometrically along the (110) and (1$\bar{1}$0) planes and healed with −OH and −H groups in a manner consistent with the expected edge surface protonation at near-neutral pH conditions (zero net proton surface charge).[48,52] Isomorphic substitutions of Mg for Al were randomly distributed in the clay particles with the condition that side-by-side substitutions were not allowed. Near-edge substitutions were avoided to minimize uncertainties associated with the parametrization of edge surface sites.[48] The number of isomorphic substitutions (114 in total) was selected to obtain a mean basal surface charge density typical of montmorillonite (about −0.1 C·m^{-2}).[53] The clay interlayers initially contained 114 Na$^+$ counterions as

required to balance the negative structural charge of the mineral. The mesopores initially contained 40 NaCl ion pairs (ionic strength $I \approx 0.6$ mol dm^{-3}) and five gas molecules (CO$_2$, CH$_4$, H$_2$, He, Ne, Ar, Kr, or Xe). The remainder of the pore space was filled with 5796 water molecules.

Interatomic interactions were described using the SPC/E water model,[54] the Smith−Dang model of Na$^+$ and Cl$^-$,[55] the CLAYFF model[56] of clay atoms, and CLAYFF-compatible parameters for clay edge O atoms.[48] Gas molecules were described using the noble-gas interaction parameters of Bourg and Sposito,[57] the EPM2 model of CO$_2$,[58] the OPLS-AA model of CH$_4$,[59] and the single-point H$_2$ model of Mondal and co-workers.[60] Interatomic interactions between unlike atomic species were predicted using the Lorentz−Berthelot combining rules. Our choice of interatomic potentials (Table S1) accurately predicts the structure and dynamics of water and gases in pure liquid water[60−64] and of water in clay interlayer nanopores[65,66] at standard temperature and pressure.

Each simulated system (one for each gas species) was equilibrated in the *NVE* ensemble for 50 ps and then in the *NVT* ensemble for 240 ps as the simulation cell size was adjusted slightly in the *y* direction to achieve a stress of $P_y = 0$ in the bulk-liquid-like water region. The eventual simulation cell size was 63.4 × 88.6 × 46.8 Å^3 in most cases, with a slightly smaller *y* dimension in the cases of Xe, CO$_2$, and CH$_4$. Each system was further equilibrated for 5 ns and then simulated for 30 ns (with a 1-fs time step) in the *NVT* ensemble at 298 K. Statistical errors were evaluated by dividing each simulation into six 5-ns blocks and treating each block as an independent replicate. Water molecules were kept rigid using the SHAKE alogorithm.[67] The clay structure was kept rigid and immobile, as in most studies of similar systems,[66,68,69] with the exception of clay H atoms. Electrostatic and dispersion interactions were computed in real space up to a distance of 15 Å; long-range electrostatic interactions were evaluated in reciprocal space using the particle−particle particle mesh (PPPM) method with an accuracy of 99.99%. Simulations were carried out using the program LAMMPS[70] and analyzed using the program VMD[71] and in-house MATLAB routines. Simulation results were analyzed to determine the coordinations, solubilities, and diffusion coefficients of the gas molecules in the mesopore (i.e., in bulk-liquid-like water) and in the interlayer nanopores. For all calculations, the mesopore was defined as the region where 70 < *y* < 85 Å, and the nanopores were defined as the region where 15 < *y* < 45 Å.

Self-diffusion coefficients *D* were calculated from the slope of a plot of the mean-square displacement l^2 versus time using the well-known Einstein relation (where *n* is the order of dimensions)

$$D = \frac{1}{2n} \lim_{t \to \infty} \frac{d\langle l^2 \rangle}{dt} \qquad (1)$$

For use in eq 1, l^2 was calculated in three dimensions in the bulk aqueous region (*n* = 3) and in the *xy* plane in the nanopores (*n* = 2). The infinite-time limit in eq 1 was approximated by calculating the slope of l^2 versus *t* at *t* = 50 ps. The constrictivity coefficient $q_{nano} = D_{nanopore}/D_{mesopore}$ was calculated to quantify the extent to which confinement influences diffusion.[65]

The relative solubilities of gas molecules in nanopore and mesopore water were calculated from the average atomic density ρ_{gas} of gas molecules in the nanopore and mesopore

regions, normalized to the density of water molecules in each region

$$K_{nano} = \frac{\rho_{gas,nano}}{\rho_{gas,meso}} \frac{\rho_{water,meso}}{\rho_{water,nano}} \qquad (2)$$

Values of K_{nano} were used to determine the free energy difference associated with the transfer of a gas molecule from mesopore to nanopore water

$$\Delta G_{meso \rightarrow nano} = -RT \ln K_{nano} \qquad (3)$$

where R is the ideal gas constant (8.3145 J mol^{-1} K^{-1}) and T is the absolute temperature.

As noted in the Introduction, the free energy associated with the dissolution of a gas molecule in liquid water is the sum of a predominantly entropic contribution associated with the formation of a hydrophobic cavity and an enthalpic contribution associated with solute–solvent interactions[22,72]

$$\Delta G_{dissolution} = \Delta G_{cavity} + \Delta G_{affinity} \qquad (4)$$

The value of $\Delta G_{affinity}$ is the sum of contributions from van der Waals and Coulomb interactions ($\Delta G_{affinity} = \Delta G_{affinity,vdW} + \Delta G_{affinity,Coulomb}$). The van der Waals contribution was calculated as

$$\Delta G_{affinity,vdW} = \sum_i N_i \left[\sum_j 4\pi\rho_j \int_{\sigma_{ij}}^{\sigma_{max}} \phi_{LJ,ij}(r)\, g_{ij}(r) r^2\, dr \right] \qquad (5)$$

where i and j represent each type of atom in the gas molecule of interest and in the surrounding solid and liquid, respectively; N_i is the number of atoms of type i per gas molecule; ρ_j is the density of atoms of type j in the simulated system; $g_{ij}(r)$ is the radial distribution function between atoms of types i and j in the region of interest; and $\phi_{LJ,ij}(r)$ is the van der Waals interaction potential between atoms of type i and j, described in our simulations by the Lennard-Jones 6–12 potential model $\{\phi_{LJ,ij}(r) = 4\varepsilon_{ij}[(\sigma_{ij}/r)^{12} - (\sigma_{ij}/r)^6]$, where ε_{ij} is the minimum in the attractive potential between atoms of type i and j and σ_{ij} is the interatomic distance at which $\phi_{LJ,ij} = 0\}$. The integral in eq 5 was calculated up to $r_{max} = 15$ Å. According to the interatomic potential models used in our simulations, the value of $\Delta G_{affinity,vdW}$ is determined predominantly by interactions with water and clay O atoms (O_w, O_{clay}) and, to a much smaller extent, with Na$^+$ and Cl$^-$ ions.

The Coulomb contributions for all gas molecules were calculated using LAMMPS in the mesopore and interlayer regions based on the relation

$$\Delta G_{affinity,Coulomb} = \sum_{ij} \frac{1}{4\pi\varepsilon_0} \frac{q_i q_j}{r_{ij}} \qquad (6)$$

where ε_0 is the permittivity of a vacuum (8.8542×10^{-12} C^2 J^{-1} m^{-1}) and q_i and q_j are the partial charges of atoms i and j, respectively, in Coulombs. The sum is calculated for all atomic pairs ij between atoms in the gas molecule of interest and atoms in the surrounding fluid or solid within a cutoff distance of 15 Å.

The free energy associated with the formation of a hydrophobic cavity was calculated by carrying out a 5-ns simulation of our system with no gas molecules present. Selected frames of the simulation (specifically, 500 frames obtained at 10-ps intervals) were analyzed to determine the probability P_0 that a sphere of radius r_{cavity}, randomly placed in the mesopore, would contain no atom. For consistency with previous studies, we used a cavity radius of $r_{cavity} = \frac{1}{2}\sigma_{ii} + r_O$, where $\frac{1}{2}\sigma_{ii}$ is the Lennard-Jones radius of the solute and r_O is the crystalline radius of oxygen.[23,72] For methane, this equation does not yield an adequate value for r_{cavity}, because methane H atoms make a significant contribution to the van der Waals radius of CH$_4$. Instead, we approximated r_{cavity,CH_4} as $r_{cavity,CH_4} = \frac{1}{2}r_{cavity,Kr} + \frac{1}{2}r_{cavity,Xe}$, because predicted gas–water radial distribution functions indicate that the effective radius of CH$_4$ in our simulations is intermediate between those of Kr and Xe. The resulting values of r_{cavity} (calculated with $r_O = 1.4$ Å[73]) for He, H$_2$, Ne, Ar, Kr, CH$_4$, and Xe are 2.790, 2.970, 2.793, 3.082, 3.212, 3.308, and 3.405 Å, respectively. For CO$_2$, we calculated the probability that two randomly placed spheres of radius $r_{cavity} = \frac{1}{2}\sigma_{Oc-Oc} + r_O = 2.917$ Å (where O$_c$ is a CO$_2$ oxygen atom) separated by the same distance as the two oxygen atoms in CO$_2$ (2.3 Å) would contain no atom. Finally, the value of ΔG_{cavity} in the mesopore region was determined for each gas solute as

$$\Delta G_{cavity} = -RT \ln P_0 \qquad (7)$$

In the interlayer region, the probability P_0 is a function not only of cavity size but also of cavity location and, in the case of CO$_2$, orientation. For all solutes except CO$_2$, the probability P_0 was determined as a function of z, with a grid spacing of 0.25 Å, across all three nanopores. Then, ΔG_{cavity} was calculated using the relation

$$\Delta G_{cavity} = -RT \ln \left[\frac{\int_{z_{max}}^{z_{min}} P_0(z)\, dz}{\Delta T_{interlayer\,water}} \right] \qquad (8)$$

where z_{min} and z_{max} are the boundaries of the MD simulation cell and $\Delta T_{interlayer\,water}$ is the equivalent thickness of water present in the interlayer region (total of 18.99 Å in the three nanopores).

For CO$_2$, the probability P_0 associated with the test insertion of a linear molecule in the nanopores was calculated for three different orientations relative to the clay surface: 0°, 45°, and 90°. The overall probability P_0 was calculated as a weighted average of the probabilities obtained for all three orientations, with the weighting being by the probability that a randomly oriented CO$_2$ molecule would form angles of 0–22.5°, 22.5–67.5°, or 67.5–90°, respectively, with the clay surface.

Adsorption Experiments. Experiments were carried out using a reference montmorillonite (SWy-1) obtained from the Clay Mineral Society's Source Clay Repository. The starting material was dispersed in deionized (DI) water, sonicated for 5 min, and centrifuged at 5000 rpm for 5 min and at 8000 rpm for 40 min to separate the 0.3–1.0-μm size fraction. The purified montmorillonite was washed repeatedly with 750 mL of 1 M NaCl solution to saturate the cation-exchange sites with Na$^+$. The homoionized material was then rinsed with DI H$_2$O/ethanol until chloride was no longer detected with a few drops of a 1 N AgNO$_3$ solution. The resulting Na-exchanged SWy-1 montmorillonite was then dried at 105 °C. The clay sample was hydrated at room temperature in a desiccator over water at ca. 85% relative humidity (RH) until a constant sample weight was reached, indicating equilibration of the 2W hydration state.

Gas adsorption in clay interlayers was measured using a gravimetric Rubotherm high-pressure magnetic suspension balance. Temperature was controlled to 0.03 K using a circulating fluid bath connected to a Pt-100 sensor near the

sample. Pressure values were recorded using Keller Preciseline transmitters with better than 0.1% full-scale (FS) accuracy. Before each measurement, the sample and measurement device were briefly evacuated using a Pfeiffer HiCube turbomolecular pump stand. The resolution of the microbalance is 10 μg, and its accuracy is better than 100 μg. All nonaqueous fluids used were research-grade, with purities of 99.99% or better. We measured the excess sorption of four nonaqueous fluids as a function of fluid pressure: Ne and Ar at 293 K and CH_4 and CO_2 at 308 K. Sample buoyancy was measured using helium, because no adsorption of helium was measurable (as confirmed by the linear decrease in sample weight with increasing helium density). Neon adsorption was too weak to detect within the uncertainty of the measurements. For Ar, CH_4, and CO_2, significant sorption was detected on the hydrated clay sample.

Sorption of gases by hydrated clay samples can take place by dissolution in interlayer water, but also on the external basal surfaces of hydrated clay stacks (tactoids). Under the simplifying assumption that dissolution in interlayer water is the predominant uptake mechanism, the measured gas surface excess n_e (moles of gas per gram of hydrated clay sample) yields the interlayer gas density ρ_{nano} (moles of gas per unit volume of nanopore water) through the relation

$$\rho_{nano} = n_e(m_{sample}/m_{clay})/V_{nano} \qquad (9)$$

where m_{sample}/m_{clay} is the mass of sample (clay plus water) per unit mass of clay (roughly 1.20 ± 0.05 g g^{-1} for the two-layer hydrate of sodium montmorillonite) and $V_{nano} = 2.42 \times 10^{-4}$ dm^3 g^{-1} is the volume of nanopore water per unit mass of clay (calculated as $V_{nano} = \frac{1}{2}a_s d_p$, where $d_p = 6.33$ Å as determined below and $a_s = 765 \pm 15$ m^2 g^{-1}).[61,74]

In the case of CH_4, the adsorption isotherm at 293 K (not shown) displays a sharp jump between 0 and 5 bar followed by a slower increase up to 150 bar, suggesting the existence of a distinct low-capacity, high-affinity uptake mechanism at low pressure. Based on the assumption that this low-pressure uptake mechanism does not correspond to dissolution in clay interlayers, we calculated interlayer gas uptake as $n_{e,interlayer} = n_e - n_{e,0}$, where $n_{e,0}$ is the contribution of the low-pressure sorption mechanism estimated by linearly extrapolating the three lowest-pressure n_e values to zero gas pressure. We used calculated values of $n_{e,interlayer}$ instead of n_e in eq 9.

Interlayer gas densities calculated with eq 9 were used to determine the free energy of gas dissolution in nanopore water as

$$\Delta G_{dissolution,nano} = -RT \ln(\rho_{nano}/\rho_{bulk}) \qquad (10)$$

where ρ_{bulk} is the density of the bulk gas phase. Finally, the free energy of dissolution in smectite interlayers at trace gas concentration was determined by linearly extrapolating the values of $\Delta G_{dissolution,nano}$ at the three lowest fluid pressures to zero fluid pressure.

■ RESULTS

Diffusion Coefficients. Simulation predictions of the diffusion coefficients of gases in the mesopore and nanopores are reported in Figure 2 and Table S2. The results are consistent (with an average deviation of 8%) with experimental data reported for aqueous solutions of 0−0.6 M NaCl at 298 K.[41,75−77] Experimental data on the D values of water and solutes in clay interlayers are scarce[66,78] but roughly consistent with the predictions obtained in the present study within the
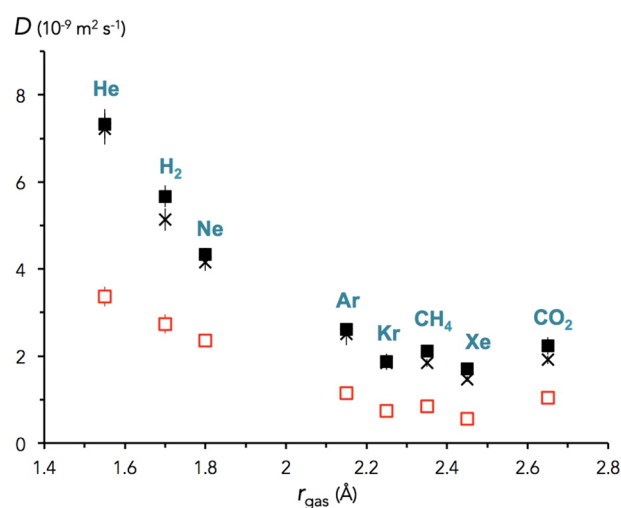

Figure 2. Self-diffusion coefficients of gas solutes as a function of solute radius. Solid black squares and open red squares show simulation predictions in the mesopore and nanopores. Black crosses show values measured in bulk liquid water.[41,77]

well-known sensitivity of MD simulations to the choice of interatomic potential parameters[79−81] and the flexibility and surface charge density of the clay sheets.[65,82] Experimental values for gas diffusion in clay interlayers do not exist, to the best of our knowledge, but previous simulation predictions[83] are consistent with our results. As expected, D values decrease with solute size and are lower in the interlayer nanopores than in bulk liquid water (Figure 2).

Values of q_{nano} derived from our simulations (Figure S1) show that nanoconfinement has a greater impact on the diffusion of gases than on that of water. This is consistent with the results described below, which show that gases have a preference for specific sites in the nanopores (in particular, sites located above the ditrigonal cavities of the siloxane surface) and must overcome a free energy barrier to travel from one such site to another, even in the case of gases such as methane that have an overall negative affinity for the nanopores.[84]

Partitioning between Mesopore and Nanopore Water. The density profiles of water, ions, and gases in the y direction (Figure 3) indicate that different gases have different relative affinities for interlayer water versus bulk liquid water. This finding contradicts the assumption that dissolved gases behave as inert tracers in water-saturated porous media. Gas density patterns show oscillations that match the pattern of hexagonal cavities on the clay surface, with an amplitude that increases with the size of the solute. These oscillations strongly suggest that gases are preferentially located above the hexagonal cavities. The influence of the clay edges on the atomic density profiles extends ∼10 Å away from the edges, both toward the mesopore and toward the interlayers. The mesopore (y = 70−85 Å) and nanopore (y = 15−45 Å) regions were defined to avoid this transition zone between the two regions.

The average concentrations of water and solutes in mesopore and nanopore water are reported in Table 1. Concentrations in nanopore water require an arbitrary definition of the width of the interlayer nanopores. Values reported in Table 1 are based on the conventional choice of water as a reference nonadsorbed species, which yields an average nanopore width of 6.33 Å. When the bulk fluid phase is humid air, water is known to adsorb on montmorillonite.[85] However, in studies where the
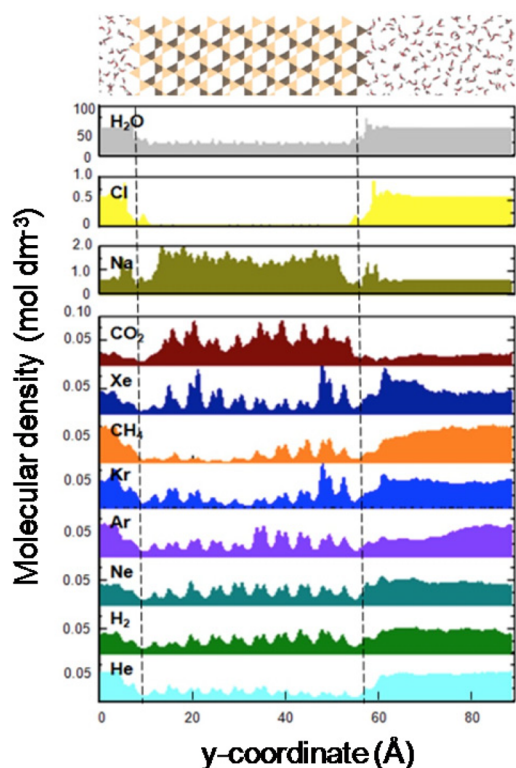
Figure 3. Atomic density profiles of water, ions, and gases in the direction normal to the clay edge surfaces. In the interlayers, local density fluctuations are aligned with the pattern of hexagonal cavities on the clay surfaces.

Figure 4. Partitioning coefficients of gas solutes between the mesopore and interlayer nanopores (K_{nano}), plotted as a function of solute radius. Dark blue squares were determined from the atomic density profiles (Table 1). Light blue squares were calculated based on hydrophobic solvation theory (Table 3).

bulk fluid phase is liquid water, water is typically treated as the reference nonadsorbed compound.[53] Further, studies that defined pore width from the perspective of the solid (i.e., as the distance between the planes of siloxane oxygens minus two times the radius of a siloxane oxygen) found that the interlayer water density is essentially equal to the density of the bulk liquid water, which is consistent with our choice of water as a reference nonadsorbed species.[65,86]

Our results reveal a nonmonotonic dependence of K_{nano} on solute radius (dark blue squares in Figure 4). The strong preference of CO_2 for the clay interlayers is consistent with previous experimental studies showing significant CO_2 adsorption in the interlayer nanopores of hydrated sodium
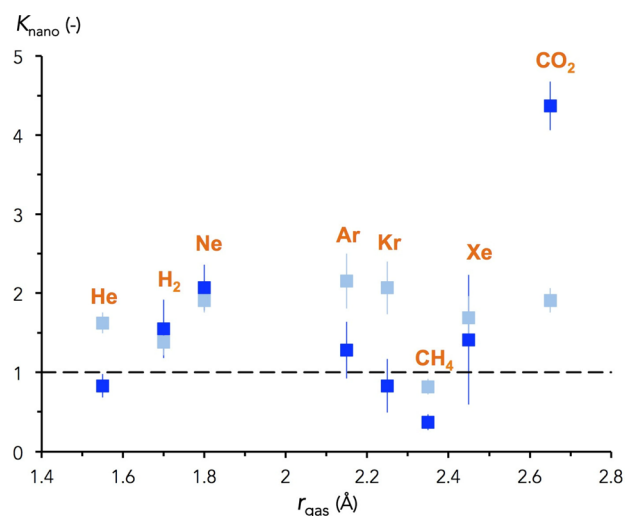
smectite[12,13,87,88] and also with previous grand canonical Monte Carlo (GCMC) simulation results yielding $K_{nano} \approx 3-7$ for the two-layer hydrate of sodium smectite at 25 or 125 bar and 348 K.[30] The relatively low affinity of CH_4 for the clay interlayers also is consistent with previous simulation results.[31] Among the other gases studied here, intermediate-size gases (Ne, H_2) have a preference for the nanopores, whereas smaller (He) and larger (CH_4) gases have a preference for the mesopore. Results for Ar, Kr, and Xe show no clear selectivity.

Coordination of Gas Solutes. First-shell coordination numbers of the gas solutes in the mesopore and interlayer nanopores were determined to identify possible correlations between coordination changes and the relative affinities of the gases for the two aqueous phases. The results are summarized in Table 2 and reported in full in the Supporting Information (Table S3).

Our results on the coordination numbers of gases in bulk liquid water are broadly consistent with previous studies.[89−91] In the mesopore, all gases tend to avoid ions ($N_{Na} = 0.25-0.35$ and $N_{Cl} = 0.15-0.21$). In the nanopores, the numbers of Na and Cl neighbors change almost exactly as expected based on

Table 1. MD Simulation Predictions of the Average Concentrations of Water and Solutes in Mesopore and Nanopore Water and Resulting Values of K_{nano} and $\Delta G_{meso \rightarrow nano}$

	$C_{mesopore}$ (mol dm^{-3})	$C_{nanopore}$ (mol dm^{-3})	K_{nano}	$\Delta G_{meso \rightarrow nano}$ (kJ mol^{-1})
H_2O	54.3 ± 0.01	54.3^a	1.0	0
Na^+	0.57 ± 0.01	3.51 ± 0.02	6.15 ± 0.15	-4.50 ± 0.06
Cl^-	0.57 ± 0.01	$\sim 0^b$	n.d.	n.d.
He	0.055 ± 0.002	0.046 ± 0.008	0.83 ± 0.15	0.46 ± 0.45
H_2	0.039 ± 0.002	0.060 ± 0.014	1.55 ± 0.37	-1.09 ± 0.60
Ne	0.039 ± 0.005	0.081 ± 0.011	2.07 ± 0.29	-1.80 ± 0.35
Ar	0.055 ± 0.008	0.070 ± 0.020	1.28 ± 0.36	-0.61 ± 0.72
Kr	0.049 ± 0.011	0.041 ± 0.017	0.83 ± 0.34	0.46 ± 1.08
CH_4	0.068 ± 0.003	0.025 ± 0.007	0.37 ± 0.10	2.46 ± 0.69
Xe	0.038 ± 0.015	0.054 ± 0.031	1.41 ± 0.82	-0.85 ± 1.65
CO_2	0.018 ± 0.005	0.079 ± 0.006	4.37 ± 0.31	-3.66 ± 0.18

^{a}Water is conventionally treated as a reference nonadsorbed species. ^{b}Interlayer Cl^- concentration was not determined as these ions are almost entirely excluded from the nanopores.[69]

Table 2. Numbers of First-Shell Oxygen Atoms (N_O) of Gases in the Mesopore and Nanopores

	$N_{O,mesopore}$	$N_{O,nanopore}$ [a]	r_{max} [b] (Å)	r_{min} [b] (Å)
He	14.5 ± 0.2	16.8 ± 0.2 (9.4, 7.4)	2.95	4.75
H_2	15.4 ± 0.2	17.4 ± 0.2 (10.2, 7.2)	3.15	4.85
Ne	16.2 ± 0.2	19.0 ± 0.2 (10.6, 8.4)	3.15	4.95
Ar	19.1 ± 0.2	21.9 ± 0.2 (12.6, 9.3)	3.55	5.25
Kr	20.2 ± 0.2	22.8 ± 0.2 (13.3, 9.5)	3.65	5.35
CH_4 [c]	21.1 ± 0.2	23.7 ± 0.2 (13.8, 9.9)	3.75	5.45
Xe	22.3 ± 0.3	25.1 ± 0.2 (14.6, 10.5)	3.85	5.55
CO_2 [c]	20.0 ± 0.2	22.7 ± 0.2 (13.1, 9.6)	4.05	5.35

[a] Values reported in parentheses are the contributions of O_w and O_{clay} atoms. [b] Locations of the first maximum and minimum of the gas−O_w radial distribution function in bulk liquid water (precision of ±0.05 Å). Values of r_{max} were identical within 0.1 Å for gas−O_{clay}. Values of r_{min} were smaller by 0.06−1.0 Å for gas−O_{clay}. For consistency, we used the same r_{min} values (last column) to calculate all gas−O coordination numbers. [c] For CH_4 and CO_2, coordination numbers were calculated based on the radial distribution functions of the C atom.

the difference in Na and Cl concentrations in the two regions (N_{Na} = 1.1−1.5, N_{Cl} = 0). With regard to the gas−oxygen coordination number N_O, our results are consistent with X-ray absorption fine structure (EXAFS) data showing that Kr has 20 water O neighbors[89] and are near the upper limit of the values determined based on neutron diffraction results (Ar, 16 ± 2;[90] CH_4, 19 ± 2[91]). Overall, as expected, predicted N_O values increase with the size of the solute. For all solutes, N_O increases by 12−17% upon transfer from the mesopore to the nanopore, indicating that the loss of first-shell O_w neighbors is more than offset by the gain of O_{clay} neighbors.

Impact of Adsorbed Ions on Gas Solubility in Nanopore Water. It is well-known that the solubilities of gases in NaCl solutions decrease with salinity.[92,93] This "salting-out" effect, related to the exclusion of Na^+ ions from the hydrophobic gas−water interface,[21] can significantly influence the solubility of gases in clay interlayer nanopores because of the high concentration of Na^+ in the nanopores (Table 1). To quantify this phenomenon, we used the fact that the three nanopores in our simulations have slightly different average Na^+ concentrations (3.40, 3.65, and 3.75 mol dm^{-3}) because of small differences in the average density of isomorphic substitutions in each clay layer.

The relative gas concentrations in each interlayer (normalized to the average value in the three interlayers) are plotted in Figure 5 as a function of interlayer Na^+ concentration. The salinity dependence of the free energy of gas dissolution in clay interlayers, calculated as RT times the slope obtained by linear regression of the data in Figure 5, equals 1.3 ± 0.8 kJ mol^{-1} M_{Na}^{-1} on average for the largest noble gases (Xe, Kr, Ar) and 0.37 ± 0.04 kJ mol^{-1} M_{Na}^{-1} for the smaller gases (Ne, H_2, He), and is insignificant for the multiatomic solutes (CH_4, CO_2).

Entropic Contribution to Gas Solubility. Uncharged or nonpolar gas solutes have a significant hydrophobic character; that is, the penalty associated with the formation of a hydrophobic cavity in liquid water (ΔG_{cavity}) contributes significantly to their overall free energy of dissolution.[17,18,22] Predicted values of ΔG_{cavity} in the mesopore and nanopores are reported in Table 3. Plots of $\ln P_0$ as a function of r_{cavity} (and also, in the interlayers, as a function of z) are shown in the Supporting Information (Figures S2−S4).

Values of ΔG_{cavity} have previously been predicted from MD simulations in the case of pure liquid water[17,20,94,95] and NaCl
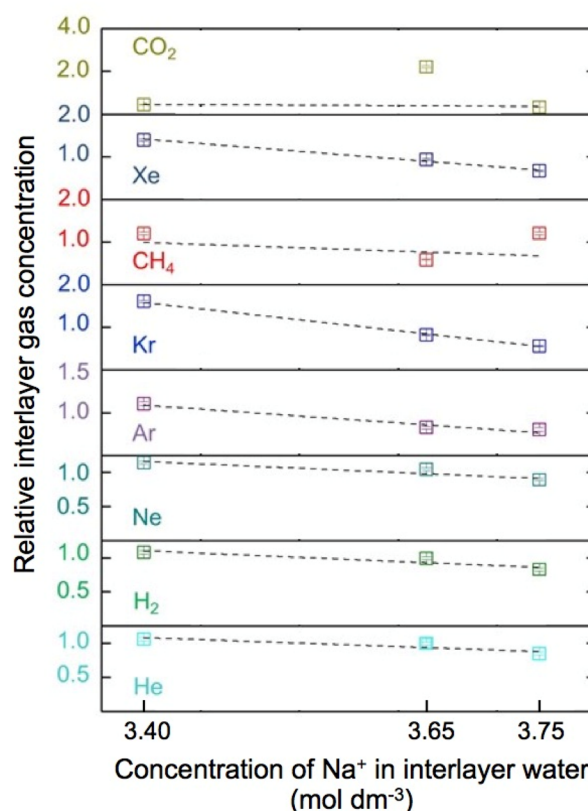
Figure 5. Relative concentration of each gas in the three interlayers, plotted as a function of interlayer Na concentration.

solutions[21,96] but not in the case of water confined in nanopores. Our results on the probability P_0 of finding an empty cavity of radius r_{cavity} in liquid water are in close agreement with those of Hummer et al.[94] and Garde et al.[20] but not with those of Sabo et al.,[95] perhaps because these authors used a smaller value for the density of bulk liquid water.

The results reported in Table 3 indicate that $\Delta G_{cavity,nanopore}$ < $\Delta G_{cavity,mesopore}$ for small gas solutes (He, H_2, Ne), whereas $\Delta G_{cavity,nanopore}$ > $\Delta G_{cavity,mesopore}$ for Kr and larger gases. In short, small cavities form more readily in clay interlayer water, whereas larger cavities form more readily in bulk liquid water. This transition is consistent with the pattern of ditrigonal cavities (i.e., hexagonal rings of O_{clay} atoms with a radius of 2.6 Å) on the siloxane surface and of a matching pattern of interfacial O_w atoms.[14,97]

In the case of CO_2, our calculations show that CO_2-shaped cavities forming angles of 0°, 45°, and 90° with the clay surface have free energies of formation ΔG_{cavity} = 29.7, 31.4, and 32.0 kJ mol^{-1}, respectively, that is, cavities sufficiently large to accommodate CO_2 occur much more readily parallel to the clay surface than at angles of 45° or 90° with respect to the clay surface. The overall entropic penalty of CO_2 solvation in the clay interlayers, ΔG_{cavity} = 30.4 kJ mol^{-1}, is dominated by the probability of formation of cavities parallel to the clay surface.

Enthalpic Contribution to Gas Solubility. As noted in the Introduction, the free energy of dissolution of a gas in water includes an enthalpic term $\Delta G_{affinity}$ associated with attractive van der Waals and Coulomb interactions between the gas solute and its surroundings. Values of $\Delta G_{affinity}$ in the mesopore and nanopores are reported in Table 3. Additional details are provided in the Supporting Information (Figures S5 and S6).

Table 3. Predicted Entropic (ΔG_{cavity}), Enthalpic ($\Delta G_{affinity}$), and Total ($\Delta G_{dissolution}$) Free Energies of Dissolution of Gases in Mesopore and Nanopore Water and Resulting Free Energies of Transfer from Mesopore to Nanopore Water ($\Delta G_{meso \to nano}$)

	mesrsopore			nanopore			
	ΔG_{cavity} (kJ mol^{-1})	$\Delta G_{affinity}$ (kJ mol^{-1})	$\Delta G_{dissolution}$ (kJ mol^{-1})	ΔG_{cavity} (kJ mol^{-1})	$\Delta G_{affinity}$ (kJ mol^{-1})	$\Delta G_{dissolution}$ (kJ mol^{-1})	$\Delta G_{meso \to nano}$ (kJ mol^{-1})
He	15.1 ± 0.0	−2.2 ± 0.0	12.9 ± 0.1	14.3 ± 0.2	−2.6 ± 0.0	11.7 ± 0.2	−1.2 ± 0.2
H$_2$	18.5 ± 0.0	−2.9 ± 0.0	15.6 ± 0.0	18.1 ± 0.3	−3.3 ± 0.0	14.8 ± 0.3	−0.8 ± 0.3
Ne	15.2 ± 0.0	−5.2 ± 0.0	10.0 ± 0.0	14.3 ± 0.2	−5.9 ± 0.0	8.4 ± 0.2	−1.6 ± 0.2
Ar	20.9 ± 0.0	−13.1 ± 0.0	7.8 ± 0.0	20.9 ± 0.4	−15.0 ± 0.0	5.9 ± 0.4	−1.9 ± 0.4
Kr	23.8 ± 0.0	−16.7 ± 0.0	7.1 ± 0.0	24.4 ± 0.3	−19.1 ± 0.1	5.3 ± 0.4	−1.8 ± 0.4
CH$_4$	26.0 ± 0.0	−18.5 ± 0.0 (−18.5/−0.0)^a	7.5 ± 0.0	27.3 ± 0.3	−19.3 ± 0.0 (−19.3/−0.1)^a	8.0 ± 0.3	0.5 ± 0.3
Xe	28.4 ± 0.0	−21.3 ± 0.0	7.1 ± 0.1	30.3 ± 0.2	−24.5 ± 0.2	5.8 ± 0.4	−1.3 ± 0.4
CO$_2$	28.8 ± 0.1	−27.6 ± 0.0 (−20.2/−7.4)^a	1.2 ± 0.1	30.4 ± 0.1	−30.8 ± 0.0 (−22.9/−7.9)^a	−0.4 ± 0.1	−1.6 ± 0.2

^{a}First and second numbers in parentheses are the contributions of van der Waals and Coulomb interactions, respectively, to $\Delta G_{affinity}$.

Our calculated values of $\Delta G_{affinity}$ are close to those reported in previous simulation studies of pure liquid water. More precisely, our results differ by 0.9 ± 1.5 kJ mol^{-1}, on average, from the values reported by Straatsma et al.[18] for Ne, Ar, and Xe and by Chandler[22] for CH$_4$. Values of $\Delta G_{affinity}$ reported in Table 3 are dominated by van der Waals interactions with O atoms in the water and solid phases and, in the case of CO$_2$, by Coulomb interactions. van der Waals interactions with Na$^+$ and Cl$^-$ ions account for less than 1.5% of $\Delta G_{affinity}$ in all cases. Coulomb interactions are insignificant in the case of methane. In the case of CO$_2$, Coulomb interactions contribute significantly to $\Delta G_{affinity}$ in each phase, but they contribute only minimally, −0.5 kJ mol^{-1}, to $\Delta G_{meso \to nano}$, indicating that the affinity of CO$_2$ for the nanopores is not primarily driven by polar interactions.

Overall, the contribution of $\Delta G_{affinity}$ to $\Delta G_{meso \to nano}$ is negative for all gases (i.e., it favors gas entry into the nanopores), predominantly because the solutes experience more attractive van der Waals interactions with O atoms in the nanopores than in bulk liquid water. This result is consistent with the greater density of O atoms in the clay structure than in water and with the greater first-shell gas−oxygen coordination number N_O in the nanopores (Table 2).

Experimental Adsorption Data. The experimental results on the uptakes of Ar, CH$_4$, and CO$_2$ from a pure gas phase onto a hydrated sodium montmorillonite sample at controlled water content (two-layer hydrate) are shown as measured surface excess (n_e) and calculated free energy of dissolution ($\Delta G_{dissolution}$) as functions of gas fluid pressure in Figure 6. Each of the three gases has a significant solubility in interlayer nanopore water that is commensurate with its solubility in bulk liquid water. The strongest uptake was measured for CO$_2$, in agreement with our simulation predictions. The sharp transition in CO$_2$ uptake at 80 bar corresponds to the phase transition from gaseous to supercritical CO$_2$. For Ar and CH$_4$, the experimental data show much weaker uptakes and steadier pressure dependences of n_e.

The conversion of the measured n_e values to calculated $\Delta G_{dissolution,nano}$ values relies on the assumption that gas uptake occurs predominantly by dissolution in clay nanopore water. This assumption is reasonable for CO$_2$ based on the preceding results. For Ar and CH$_4$, gas uptake in clay interlayers is sufficiently weak that other processes might contribute significantly to n_e. The free energies of dissolution reported
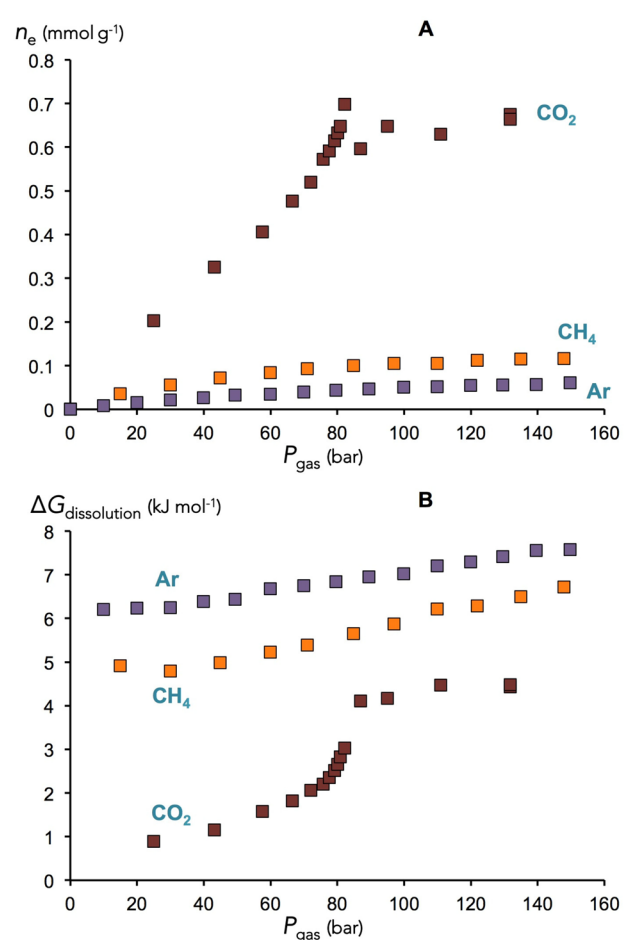

Figure 6. Uptakes of Ar, CH$_4$, and CO$_2$ by hydrated sodium montmorillonite (two-layer hydrate) from a pure gas phase, plotted as a function of gas pressure: (a) measured surface excess, n_e, and (b) calculated free energy of dissolution in clay interlayer water, $\Delta G_{dissolution,nano}$.

in Figure 6b, therefore, might constitute only lower boundaries to the true values of $\Delta G_{dissolution,nano}$.

■ DISCUSSION

Gas Solubility in Mesopore Water. The values of $\Delta G_{dissolution}$ in the mesopore reported in Table 3 are directly comparable to previous experimental[33−40] and simula-

tion[17,19,95,98−103] results on gas solubility in bulk liquid water (Table 4). The experimental values of $\Delta G_{dissolution}$ are more

Table 4. Predicted Free Energies of Dissolution of Gases in Mesopore Water ($\Delta G_{dissolution}$, kJ mol^{-1}) and Comparison with Previous Experimental and Simulation Results

	simulations (this study)	experiments[a]	previous simulations[‡]
He	12.9 ± 0.1	11.6[33]/11.9[34]	7.1−7.6[99]
H$_2$	15.6 ± 0.0	9.8[33]/10.2[38]	8.7−9.2[95]
Ne	10.0 ± 0.0	11.2[33]/11.6[34]	9.0−11.8[72,99,100,102]
Ar	7.8 ± 0.0	8.4[33]/9.0[35]	7.8−10.2[72,99,100,102]
Kr	7.1 ± 0.0	6.9[33]/7.6[36]	6.6−8.5[72,100,102]
CH$_4$	7.5 ± 0.0	8.4[33]/8.6[39]	7.7−15.4[72,98−103]
Xe	7.1 ± 0.1	5.6[33]/6.3[37]	3.3−8.2[72,100]
CO$_2$	1.2 ± 0.1	0.9[33]/0.7[40]	0.2−4.4[17]

[a]First and second listed values were reported for pure water and 0.6 M NaCl solutions, respectively (or, almost equivalently, seawater). Confidence intervals are ±0.2 or less. [‡]Previous simulation results were obtained using the Widom particle insertion (PI) or thermodynamic integration (TI) methods for gases in pure water or 1.0 M NaCl solutions using a range of interatomic potential models at 298 or 300 K.

positive by 0.4 ± 0.2 kJ mol^{-1}, on average, in 0.6 M NaCl solution than in pure liquid water. Based on the data in Table 5,

Table 5. Predicted and Measured Free Energies of Dissolution of Gases in Clay Nanopore Water ($\Delta G_{dissolution}$, kJ mol^{-1})

	simulations (this study)	experiments (this study)
He	11.7 ± 0.2	
H$_2$	14.8 ± 0.3	
Ne	8.4 ± 0.2	
Ar	5.9 ± 0.4	6.2 ± 0.3[a]
Kr	5.3 ± 0.4	
CH$_4$	8.0 ± 0.3	4.8 ± 0.3[a,b]
Xe	5.8 ± 0.4	
CO$_2$	−0.4 ± 0.1	0.3 ± 0.3[a]

[a]Confidence intervals on our experimental values were estimated from the linear extrapolation to zero pressure and from the uncertainty in m_{sample}/m_{clay}. [b]Experimental values for $\Delta G_{dissolution}$ were calculated under the assumption that dissolution in nanopore water is the predominant mechanism of gas uptake on hydrated clay; comparison with our simulation predictions suggests that this assumption is likely incorrect in the case of CH$_4$.

the salinity dependence of $\Delta G_{dissolution}$ is 1.1 ± 0.2 kJ mol^{-1} M_{NaCl}^{-1} for the large noble gases (Xe, Kr, Ar), 0.6 ± 0.1 kJ mol^{-1} M_{NaCl}^{-1} for the smaller monatomic gases (He, H$_2$, Ne), and almost zero for CH$_4$ and CO$_2$. These values are close to those derived from the results in Figure 5, indicating that adsorbed Na$^+$ in nanopore water and dissolved NaCl in bulk liquid water cause remarkably similar salting-out effects in the case of dissolved gases.

Overall, our simulations correctly predict the decrease in $\Delta G_{dissolution}$ with increasing solute size.[35−38,40,104] The predicted free energies of dissolution of gases in bulk liquid water are within 0.5−1.6 kJ mol^{-1} of the experimental values except for that of H$_2$. This agreement compares favorably with the precision achieved in previous MD simulation studies (with differences as large as 4.9 kJ mol^{-1} in the case of Xe[18,72,100] and 7.6 kJ mol^{-1} in the case of CH$_4$).[72,98] The significant scatter of

previous simulation predictions reflects the sensitivity of the predicted energies to the choice of interatomic potential parameters, as well as the difficulty of precisely predicting $\Delta G_{dissolution}$ for larger gases, particularly in older studies.[72] Other details of the simulation predictions likely play a much smaller role. For example, explicit treatment of gas polarizability increases gas solubility in ambient liquid water by only ∼1.0 kJ mol^{-1} for Xe and much less for the smaller noble gases.[72] Long-range dispersion interactions beyond the cutoff of 15 Å, which are neglected in our simulations, contribute less than 0.1 kJ mol^{-1} to gas solubility according to the Born solvation model.[95] Overall, the interatomic potential parameters used here yield reasonable predictions of the energetics of gas dissolution in water except in the case of H$_2$.

Gas Solubility in Nanopore Water. The values of $\Delta G_{dissolution}$ in the clay nanopores reported in Table 3 are directly comparable to the results of our gravimetric adsorption experiments in the limit of near-zero gas pressure (Table 5, Figure 6). Our simulation predictions and experimental results on the solubility of gases in sodium smectite interlayer nanopores are broadly consistent in the cases of CO$_2$ and Ar, but they differ by ∼3 kJ mol^{-1} in the case of CH$_4$. The discrepancy observed for CH$_4$ suggests that methane uptake in our experiments might be dominated by a process other than dissolution in interlayer water.

Figure 7 provides a graphical summary of the solubility data reported in Tables 4 and 5. The figure highlights the rough
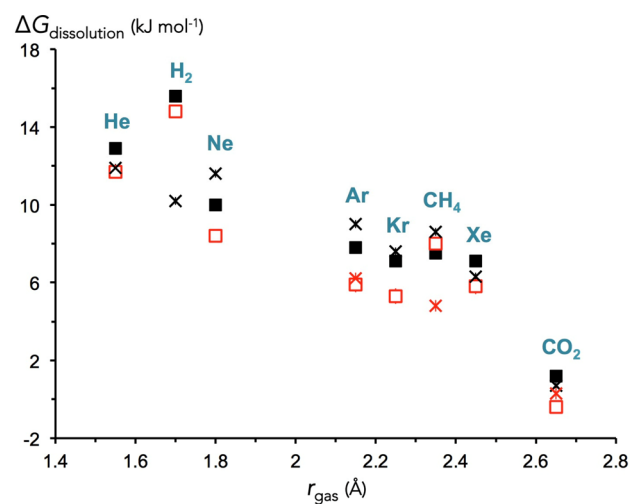

Figure 7. Predicted (squares) and measured (crosses) free energies of dissolution of gases in bulk liquid water (black) and interlayer water (red), plotted as a function of solute radius. Error bars are smaller than the symbols. In the case of the simulation predictions, the error bars describe only the statistical error, not the systematic error associated with the choice of interatomic potential parameters.

agreement (in most cases, within about 2 kJ mol^{-1}) between the simulation predictions and experimental results on gas solvation energetics in bulk and nanopore water. The only major disagreements are observed in the cases of H$_2$ (for which the use of a single-point model for H$_2$ is a possible source of discrepancy) and CH$_4$ in clay interlayers. The figure indicates that at least four gases (Ne, Ar, Kr, CO$_2$) have greater solubilities in clay interlayer water than in bulk liquid water.

Relative Solubility of Gases in Mesopore versus Nanopore Water. The values of ΔG_{cavity} and $\Delta G_{affinity}$ predicted in the present study (Table 3, Figure 8) provide
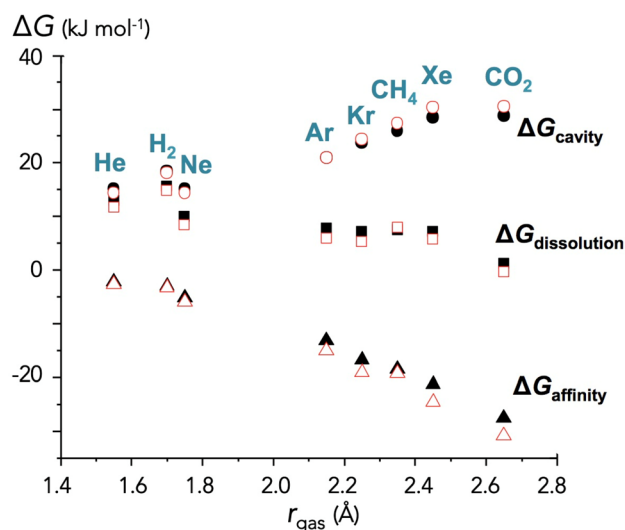
Figure 8. Predicted enthalpic, entropic, and overall free energies of dissolution of gases in mesopore water (solid black symbols) and nanopore water (open red symbols), plotted as a function of solute radius. Error bars (statistical uncertainties) are smaller than the symbols.

insight into the fundamental basis of the gas partitioning between bulk liquid water and clay interlayer nanopores. In particular, our results show that the affinity term, $\Delta G_{affinity}$, always favors gas partitioning into nanopore water. This attraction is strongly modulated by the entropic term, ΔG_{cavity}, which inhibits the formation of large hydrophobic cavities (particularly large spherical cavities) at the clay–water interface while facilitating the formation of smaller cavities.

The relative affinities of gases for the mesopore and interlayer nanopores ($\Delta G_{meso \rightarrow nano}$) were calculated both directly from the partitioning coefficient K_{nano} (Table 1) and indirectly from the values of ΔG_{cavity} and $\Delta G_{affinity}$ in each phase (Table 3). The free energies calculated using the two approaches are identical, within error, for H_2, Ne, and Xe. For the other gases, the two methods yield qualitatively consistent trends but only rough quantitative agreement (within ~2 kJ mol^{-1}). The partition coefficients K_{nano} corresponding to both sets of values of $\Delta G_{meso \rightarrow nano}$ are shown in Figure 4.

The differences between direct and indirect calculations of $\Delta G_{meso \rightarrow nano}$ have several possible origins. In particular, the error bars in the direct calculations of $\Delta G_{meso \rightarrow nano}$ (Table 1) might underestimate the uncertainty of the predicted values if the residence times of the gases in the nanopores or mesopores are similar to or greater than the 5-ns time interval used to estimate the statistical uncertainty of predicted values. A second possible source of discrepancy, in the case of CO_2, is that long-range Coulomb interactions (beyond 15 Å) are taken into account in the direct calculations but not in the indirect calculations. Despite these potential sources of discrepancy, the similarity between direct and indirect values of $\Delta G_{meso \rightarrow nano}$ is sufficiently strong to suggest that gas dissolution in nanopore water is well-described by hydrophobic solvation theory.

Implications for Gas Transport in Subsurface Environments. An important geochemical implication of our results is that dissolved gases do not generally behave as inert tracers in clay-rich sedimentary rocks. In particular, our results indicate that Ne, Ar, Kr, and CO_2 likely have greater solubilities in the pore space of fine-grained rocks than in bulk liquid water. This

finding might shed light on the observation that fluids in sedimentary basins are often enriched in either heavy (Kr, Xe) or light noble (Ne) noble gases or both.[2,105,106] Our results might also provide insight into the presence of excess Ar in layered silicate minerals such as biotite and gauconite, with potential implications for K–Ar geochronology,[107,108] and into the uptake of He and Ne in amphibole, with potential implications for the recycling flux of noble gases to the mantle.[109] Finally, one implication of the present research is that changes in nanopore width during sediment burial can give rise to spatial and temporal variations in gas solubility.

CONCLUDING REMARKS

The partitioning and diffusion behaviors of noble gases, H_2, CH_4, and CO_2 in bulk liquid water and nanoconfined aqueous fluids were determined using molecular dynamics simulations and gravimetric adsorption experiments. Our results on the self-diffusion, coordination, and solubility of gases in bulk liquid water are broadly consistent with experimental data, with a few notable exceptions. Our predictions on the relative solubilities of gases in clay interlayer water compared to bulk liquid water are consistent with hydrophobic solvation theory. Overall, our results strongly suggest that dissolved gases do not generally behave as inert tracers of fluid migration in the subsurface, particularly in fine-grained sedimentary rocks. Instead, they exhibit a distinct preference either for bulk-liquid-like water or for clay interlayer nanopore water, with potential implications for the interpretation of field-scale experimental results on the migration of dissolved gases in clay-rich sediments and sedimentary rocks.

ASSOCIATED CONTENT

Supporting Information

The Supporting Information is available free of charge on the ACS Publications website at DOI: 10.1021/acs.jpcc.7b09768.

Additional detail on the MD simulation results (PDF)

AUTHOR INFORMATION

Corresponding Authors
*E-mail: bourg@princeton.edu.
*E-mail: gadikota@wisc.edu.

ORCID

Greeshma Gadikota: 0000-0002-6527-8316
Gernot Rother: 0000-0003-4921-6294
Michael C. Cheshire: 0000-0003-1792-6881
Ian C. Bourg: 0000-0002-5265-7229

Author Contributions

The manuscript was written primarily by G.G. and I.C.B. based on contributions of all authors, G.G. carried out the MD simulations, B.D. contributed to the analysis of MD simulation trajectories, and G.R. and M.C.C. carried out the gas adsorption experiments.

Notes

The authors declare no competing financial interest.

ACKNOWLEDGMENTS

■ REFERENCES

(1) Darrah, T. H.; Vengosh, A.; Jackson, R. B.; Warner, N. R.; Poreda, R. J. Noble Gases Identify the Mechanisms of Fugitive Gas Contamination in Drinking-Water Wells Overlying the Marcellus and Barnett Shales. *Proc. Natl. Acad. Sci. U. S. A.* **2014**, *111*, 14076−14081.

(2) Castro, M. C.; Jambon, A.; de Marsily, G.; Schlosser, P. Noble Gases as Natural Tracers of Water Circulation in the Paris Basin: 1. Measurements and Discussion of Their Origin and Mechanisms of Vertical Transport in the Basin. *Water Resour. Res.* **1998**, *34*, 2443−2466.

(3) Gilfillan, S. M. V.; Sherwood Lollar, B.; Holland, G.; Blagburn, D.; Stevens, S.; Schoell, M.; Cassidy, M.; Ding, Z.; Zhou, Z.; Lacrampe-Couloume, G.; et al. Solubility Trapping in Formation Water as Dominant CO_2 Sink in Natural Gas Fields. *Nature* **2009**, *458*, 614−618.

(4) Sathaye, K. J.; Larson, T. E.; Hesse, M. A. Noble Gas Fractionation during Subsurface Gas Migration. *Earth Planet. Sci. Lett.* **2016**, *450*, 1−9.

(5) Busch, A.; Bertier, P.; Gensterblum, Y.; Rother, G.; Spiers, C. J.; Zhang, M.; Wentinck, H. M. On Sorption and Swelling of CO_2 in Clays. *Geomech. Geophys. Geo-Energy Geo-Resources* **2016**, *2*, 111−130.

(6) Horseman, S. T.; Harrington, J. F.; Sellin, P. Gas Migration in Clay Barriers. *Eng. Geol.* **1999**, *54*, 139−149.

(7) Didier, M.; Leone, L.; Greneche, J.-M.; Giffaut, E.; Charlet, L. Adsorption of Hydrogen Gas and Redox Processes in Clays. *Environ. Sci. Technol.* **2012**, *46*, 3574−3579.

(8) Jiang, J.; Shao, Y.; Younis, R. M. Development of a Multi-Continuum Multi-Component Model for Enhanced Gas Recovery and CO_2 Storage in Fractured Shale Gas Reservoirs. Presented at the *SPE Improved Oil Recovery Symposium*, Tulsa, OK, Apr 12−14, 2014.

(9) Gandossi, L. *An Overview of Hydraulic Fracturing and Other Formation Stimulation Technologies for Shale Gas Production*; Report EUR 26347 EN; European Commisison Joint Research Centre: Petten, The Netherlands, 2013.

(10) Pacala, S.; Socolow, R. Stabilization Wedges: Solving the Climate Problem for the next 50 Years with Current Technologies. *Science* **2004**, *305*, 968−972.

(11) Bourg, I. C. Sealing Shales versus Brittle Shales: A Sharp Threshold in the Material Properties and Energy Technology Uses of Fine-Grained Sedimentary Rocks. *Environ. Sci. Technol. Lett.* **2015**, *2*, 255−259.

(12) Loring, J. S.; Schaef, H. T.; Turcu, R. V. F.; Thompson, C. J.; Miller, Q. R. S.; Martin, P. F.; Hu, J.; Hoyt, D. W.; Qafoku, O.; Ilton, E. S.; et al. In Situ Molecular Spectroscopic Evidence for CO_2 Intercalation into Montmorillonite in Supercritical Carbon Dioxide. *Langmuir* **2012**, *28*, 7125−7128.

(13) Loring, J. S.; Ilton, E. S.; Chen, J.; Thompson, C. J.; Martin, P. F.; Bénézeth, P.; Rosso, K. M.; Felmy, A. R.; Schaef, H. T. In Situ Study of CO_2 and H_2O Partitioning between Na-Montmorillonite and Variably Wet Supercritical Carbon Dioxide. *Langmuir* **2014**, *30*, 6120−6128.

(14) Botan, A.; Rotenberg, B.; Marry, V.; Turq, P.; Noetinger, B. Carbon Dioxide in Montmorillonite Clay Hydrates: Thermodynamics, Structure, and Transport from Molecular Simulation. *J. Phys. Chem. C* **2010**, *114*, 14962−14969.

(15) Kuila, U.; Prasad, M. Specific Surface Area and Pore-Size Distribution in Clays and Shales. *Geophys. Prospect.* **2013**, *61*, 341−362.

(16) Keller, L. M.; Schuetz, P.; Erni, R.; Rossell, M. D.; Lucas, F.; Gasser, P.; Holzer, L. Characterization of Multi-Scale Microstructural Features in Opalinus Clay. *Microporous Mesoporous Mater.* **2013**, *170*, 83−94.

(17) Jiao, D.; Rempe, S. B. CO_2 Solvation Free Energy Using Quasi-Chemical Theory. *J. Chem. Phys.* **2011**, *134*, 224506.

(18) Straatsma, T. P.; Berendsen, H. J. C.; Postma, J. P. M. Free Energy of Hydrophobic Hydration: A Molecular Dynamics Study of Noble Gases in Water. *J. Chem. Phys.* **1986**, *85*, 6720−6727.

(19) Guillot, B.; Guissani, Y. Temperature Dependence of the Solubility of Non-Polar Gases in Liquids. *Mol. Phys.* **1993**, *79*, 53−75.

(20) Garde, S.; Hummer, G.; García, A. E.; Paulaitis, M. E.; Pratt, L. R. Origin of Entropy Convergence in Hydrophobic Hydration and Protein Folding. *Phys. Rev. Lett.* **1996**, *77*, 4966−4968.

(21) Hummer, G.; Garde, S.; Garcia, A. E.; Pratt, L. R. New Perspectives on Hydrophobic Effects. *Chem. Phys.* **2000**, *258*, 349−370.

(22) Chandler, D. Interfaces and the Driving Force of Hydrophobic Assembly. *Nature* **2005**, *437*, 640−647.

(23) Pratt, L. R.; Chandler, D. Theory of the Hydrophobic Effect. *J. Chem. Phys.* **1977**, *67*, 3683−3704.

(24) Greenwell, H. C.; Jones, W.; Coveney, P. V.; Stackhouse, S. On the Application of Computer Simulation Techniques to Anionic and Cationic Clays: A Materials Chemistry Perspective. *J. Mater. Chem.* **2006**, *16*, 708−723.

(25) Sposito, G.; Skipper, N. T.; Sutton, R.; Park, S.-H.; Soper, A. K.; Greathouse, J. A. Surface Geochemistry of the Clay Minerals. *Proc. Natl. Acad. Sci. U. S. A.* **1999**, *96*, 3358−3364.

(26) Cygan, R. T.; Greathouse, J. A.; Heinz, H.; Kalinichev, A. G. Molecular Models and Simulations of Layered Materials. *J. Mater. Chem.* **2009**, *19*, 2470−2481.

(27) Aljama, H.; Wilcox, J. Microscopic Diffusion of CO_2 in Clay Nanopores. *Chem. Phys. Lett.* **2017**, *677*, 162−166.

(28) Cygan, R. T.; Guggenheim, S.; Koster van Groos, A. F. Molecular Models for the Intercalation of Methane Hydrate Complexes in Montmorillonite Clay. *J. Phys. Chem. B* **2004**, *108*, 15141−15149.

(29) Park, S.-H.; Sposito, G. Do Montmorillonite Surfaces Promote Methane Hydrate Formation? Monte Carlo and Molecular Dynamics Simulations. *J. Phys. Chem. B* **2003**, *107*, 2281−2290.

(30) Botan, A.; Rotenberg, B.; Marry, V.; Turq, P.; Noetinger, B. Carbon Dioxide in Montmorillonite Clay Hydrates: Thermodynamics, Structure, and Transport from Molecular Simulation. *J. Phys. Chem. C* **2010**, *114*, 14962−14969.

(31) Rao, Q.; Leng, Y. Methane Aqueous Fluids in Montmorillonite Clay Interlayer under near-Surface Geological Conditions: A Grand Canonical Monte Carlo and Molecular Dynamics Simulation Study. *J. Phys. Chem. B* **2014**, *118*, 10956−10965.

(32) Rao, Q.; Leng, Y. Molecular Understanding of CO_2 and H_2O in Montmorillonite Clay Interlayer under CO_2 Geological Sequestration Conditions. *J. Phys. Chem. C* **2016**, *120*, 2642−2654.

(33) Wilhelm, E.; Battino, R.; Wilcock, R. J. Low-Pressure Solubility of Gases in Liquid Water. *Chem. Rev.* **1977**, *77*, 219−262.

(34) Weiss, R. F. Solubility of Helium and Neon in Water and Seawater. *J. Chem. Eng. Data* **1971**, *16*, 235−241.

(35) Clever, H. L.; Holland, C. J. Solubility of Argon Gas in Aqueous Alkali Halide Solutions: Temperature Coefficient of the Salting Out Parameter. *J. Chem. Eng. Data* **1968**, *13*, 411−414.

(36) Weiss, R. F.; Kyser, T. K. Solubility of Krypton in Water and Seawater. *J. Chem. Eng. Data* **1978**, *23*, 69−72.

(37) Clever, H. L. *Solubility Data Series: Krypton, Xenon, and Radon - Gas Solubilities*; Pergamon Press: Elmsford, NY, 1979; Vol. 2.

(38) Crozier, T. E.; Yamamoto, S. Solubility of Hydrogen in Water, Seawater, and NaCl Solutions. *J. Chem. Eng. Data* **1974**, *19*, 242−244.

(39) Ben-Naim, A.; Yaacobi, M. Effects of Solutes on the Strength of Hydrophobic Interaction and Its Temperature Dependence. *J. Phys. Chem.* **1974**, *78*, 170−175.

(40) Weiss, R. F. Carbon Dioxide in Water and Seawater: The Solubility of a Non-Ideal Gas. *Mar. Chem.* **1974**, *2*, 203−215.

(41) Jähne, B.; Heinz, G.; Dietrich, W. Measurement of the Diffusion Coefficients of Sparingly Soluble Gases in Water. *J. Geophys. Res.* **1987**, *92*, 10767−10776.

(42) Aggarwal, V.; Chien, Y.-Y.; Teppen, B. J. Molecular Simulations to Estimate Thermodynamics for Adsorption of Polar Organic Solutes to Montmorillonite. *Eur. J. Soil Sci.* **2007**, *58*, 945−957.

(43) Laird, D. A.; Shang, C. Relationship between Cation Exchange Selectivity and Crystalline Swelling in Expanding 2:1 Phyllosilicates. *Clays Clay Miner.* **1997**, *45*, 681−689.

(44) Schauperl, M.; Podewitz, M.; Waldner, B. J.; Liedl, K. R. Enthalpic and Entropic Contributions to Hydrophobicity. *J. Chem. Theory Comput.* **2016**, *12*, 4600−4610.

(45) Allen-King, R. M.; Grathwohl, P.; Ball, W. P. New Modeling Paradigms for the Sorption of Hydrophobic Organic Chemicals to Heterogeneous Carbonaceous Matter in Soils, Sediments, and Rocks. *Adv. Water Resour.* **2002**, *25*, 985−1016.

(46) Sulman, B. N.; Phillips, R. P.; Oishi, A. C.; Shevliakova, E.; Pacala, S. W. Microbe-Driven Turnover Offsets Mineral-Mediated Storage of Soil Carbon under Elevated CO_2. *Nat. Clim. Change* **2014**, *4*, 1099−1102.

(47) Jolin, W. C.; Goyetche, R.; Carter, K.; Medina, J.; Vasudevan, D.; Mackay, A. A. Predicting Organic Cation Sorption Coefficients: Accounting for Competition from Sorbed Inorganic Cations Using a Simple Probe Molecule. *Environ. Sci. Technol.* **2017**, *51*, 6193−6201.

(48) Tournassat, C.; Bourg, I. C.; Holmboe, M.; Sposito, G.; Steefel, C. I. Molecular Dynamics Simulations of Anion Exclusion in Clay Interlayer Nanopores. *Clays Clay Miner.* **2016**, *64*, 374−388.

(49) Honorio, T.; Brochard, L.; Vandamme, M. Hydration Phase Diagram of Clay Particles from Molecular Simulations. *Langmuir* **2017**, *33*, 12766−12776.

(50) Brown, K. M.; Poeppe, D.; Josh, M.; Sample, J.; Even, E.; Saffer, D.; Tobin, H.; Hirose, T.; Kulongoski, J. T.; Toczko, S.; et al. The Action of Water Films at Å-Scales in the Earth: Implications for the Nankai Subduction System. *Earth Planet. Sci. Lett.* **2017**, *463*, 266−276.

(51) Tsipursky, S. I.; Drits, V. A. The Distribution of Octahedral Cations in the 2:1 Layers of Dioctahedral Smectites Studied by Oblique-Texture Electron Diffraction. *Clay Miner.* **1984**, *19*, 177−193.

(52) Churakov, S. V. Ab Initio Study of Sorption on Pyrophyllite: Structure and Acidity of the Edge Sites. *J. Phys. Chem. B* **2006**, *110*, 4135−4146.

(53) Sposito, G. *The Surface Chemistry of Soils*; Oxford University Press: New York, 1984.

(54) Berendsen, H. J. C.; Grigera, J. R.; Straatsma, T. P. The Missing Term in Effective Pair Potentials. *J. Phys. Chem.* **1987**, *91*, 6269−6271.

(55) Smith, D. E.; Dang, L. X. Computer Simulations of NaCl Association in Polarizable Water. *J. Chem. Phys.* **1994**, *100*, 3757−3766.

(56) Cygan, R. T.; Liang, J.-J.; Kalinichev, A. G. Molecular Models of Hydroxide, Oxyhydroxide, and Clay Phases and the Development of a General Force Field. *J. Phys. Chem. B* **2004**, *108*, 1255−1266.

(57) Bourg, I. C.; Sposito, G. Isotopic Fractionation of Noble Gases by Diffusion in Liquid Water: Molecular Dynamics Simulations and Hydrologic Applications. *Geochim. Cosmochim. Acta* **2008**, *72*, 2237−2247.

(58) Harris, J. G.; Yung, K. H. Carbon Dioxide's Liquid-Vapor Coexistence Curve and Critical Properties as Predicted by a Simple Molecular Model. *J. Phys. Chem.* **1995**, *99*, 12021−12024.

(59) Jorgensen, W. L.; Maxwell, D. S.; Tirado-Rives, J. Development and Testing of the OPLS All-Atom Force Field on Conformational Energetics and Properties of Organic Liquids. *J. Am. Chem. Soc.* **1996**, *118*, 11225−11236.

(60) Mondal, S.; Ghosh, S.; Chattaraj, P. K. A Molecular Dynamics Study on sI Hydrogen Hydrate. *J. Mol. Model.* **2013**, *19*, 2785−2790.

(61) Sabo, D.; Rempe, S. B.; Greathouse, J. A.; Martin, M. G. Molecular Studies of the Structural Properties of Hydrogen Gas in Bulk Water. *Mol. Simul.* **2006**, *32*, 269−278.

(62) Hura, G.; Russo, D.; Glaeser, R. M.; Head-Gordon, T.; Krack, M.; Parrinello, M. Water Structure as a Function of Temperature from

X-Ray Scattering Experiments and Ab Initio Molecular Dynamics. *Phys. Chem. Chem. Phys.* **2003**, *5*, 1981−1991.

(63) Wasserman, E.; Wood, B.; Brodholt, J. The Static Dielectric Constant of Water at Pressures up to 20 kbar and Temperatures to 1273 K: Experiment, Simulations, and Empirical Equations. *Geochim. Cosmochim. Acta* **1995**, *59*, 1−6.

(64) Bourg, I. C.; Richter, F. M.; Christensen, J. N.; Sposito, G. Isotopic Mass Dependence of Metal Cation Diffusion Coefficients in Liquid Water. *Geochim. Cosmochim. Acta* **2010**, *74*, 2249−2256.

(65) Holmboe, M.; Bourg, I. C. Molecular Dynamics Simulations of Water and Sodium Diffusion in Smectite Interlayer Nanopores as a Function of Pore Size and Temperature. *J. Phys. Chem. C* **2014**, *118*, 1001−1013.

(66) Bourg, I. C.; Sposito, G. Connecting the Molecular Scale to the Continuum Scale for Diffusion Processes in Smectite-Rich Porous Media. *Environ. Sci. Technol.* **2010**, *44*, 2085−2091.

(67) Ryckaert, J.-P.; Ciccotti, G.; Berendsen, H. J. C. Numerical Integration of the Cartesian Equations of Motion of a System with Constraints: Molecular Dynamics of N-Alkanes. *J. Comput. Phys.* **1977**, *23*, 327−341.

(68) Rotenberg, B.; Marry, V.; Vuilleumier, R.; Malikova, N.; Simon, C.; Turq, P. Water and Ions in Clays: Unraveling the Interlayer/micropore Exchange Using Molecular Dynamics. *Geochim. Cosmochim. Acta* **2007**, *71*, 5089−5101.

(69) Hsiao, Y.-W.; Hedström, M. Molecular Dynamics Simulations of NaCl Permeation in Bihydrated Montmorillonite Interlayer Nanopores. *J. Phys. Chem. C* **2015**, *119*, 17352−17361.

(70) Plimpton, S. Fast Parallel Algorithms for Short-Range Molecular Dynamics. *J. Comput. Phys.* **1995**, *117*, 1−19.

(71) Humphrey, W.; Dalke, A.; Schulten, K. VMD: Visual Molecular Dynamics. *J. Mol. Graphics* **1996**, *14*, 33−38.

(72) Guillot, B.; Guissani, Y. A Computer Simulation Study of the Temperature Dependence of the Hydrophobic Hydration. *J. Chem. Phys.* **1993**, *99*, 8075−8094.

(73) Graziano, G. Shedding Light on the Hydrophobicity Puzzle. *Pure Appl. Chem.* **2016**, *88*, 177−188.

(74) Tournassat, C.; Bourg, I. C.; Steefel, C. I.; Bergaya, F. Surface Properties of Clay Minerals. *Dev. Clay Sci.* **2015**, *6*, 5−31.

(75) Mills, R. Self-Diffusion In Normal and Heavy Water in the Range 1−45°. *J. Phys. Chem.* **1973**, *77*, 685−688.

(76) Poisson, A.; Papaud, A. Diffusion Coefficients of Major Ions in Seawater. *Mar. Chem.* **1983**, *13*, 265−280.

(77) Wise, D. L.; Houghton, G. The Diffusion Coefficients of Ten Slightly Soluble Gases in Water at 10−60°C. *Chem. Eng. Sci.* **1966**, *21*, 999−1010.

(78) Marry, V.; Dubois, E.; Malikova, N.; Breu, J.; Haussler, W. Anisotropy of Water Dynamics in Clays: Insights from Molecular Simulations for Experimental QENS Analysis. *J. Phys. Chem. C* **2013**, *117*, 15106−15115.

(79) Warr, O.; Ballentine, C. J.; Mu, J.; Masters, A. Optimizing Noble Gas-Water Interactions via Monte Carlo Simulations. *J. Phys. Chem. B* **2015**, *119*, 14486−14495.

(80) Jiang, H.; Economou, I. G.; Panagiotopoulos, A. Z. Molecular Modeling of Thermodynamic and Transport Properties for CO_2 and Aqueous Brines. *Acc. Chem. Res.* **2017**, *50*, 751−758.

(81) Hamm, L. M.; Bourg, I. C.; Wallace, A. F.; Rotenberg, B. Molecular Simulation of CO_2-and CO_3-Brine-Mineral Systems. *Rev. Mineral. Geochem.* **2013**, *77*, 189−228.

(82) Greathouse, J. A.; Cygan, R. T.; Fredrich, J. T.; Jerauld, G. R. Molecular Dynamics Simulation of Diffusion and Electrical Conductivity in Montmorillonite Interlayers. *J. Phys. Chem. C* **2016**, *120*, 1640−1649.

(83) Titiloye, J. O.; Skipper, N. T. Computer Simulation of the Structure and Dynamics of Methane in Hydrated Na-Smectite Clay. *Chem. Phys. Lett.* **2000**, *329*, 23−28.

(84) Bui, T.; Phan, A.; Cole, D. R.; Striolo, A. Transport Mechanism of Guest Methane in Water-Filled Nanopores. *J. Phys. Chem. C* **2017**, *121*, 15675−15686.

(85) Cases, J. M.; Bérend, I.; Besson, G.; Francois, M.; Uriot, J. P.; Thomas, F.; Poirier, J. E. Mechanism of Adsorption and Desorption of Water Vapor by Homoionic Montmorillonite. 1. The Sodium-Exchanged Form. *Langmuir* **1992**, *8*, 2730−2739.

(86) Bourg, I. C.; Sposito, G. Molecular Dynamics Simulations of the Electrical Double Layer on Smectite Surfaces Contacting Concentrated Mixed Electrolyte (NaCl − CaCl₂) Solutions. *J. Colloid Interface Sci.* **2011**, *360*, 701−715.

(87) Ilton, E. S.; Schaef, H. T.; Qafoku, O.; Rosso, K. M.; Felmy, A. R. In Situ X-Ray Diffraction Study of Na⁺ Saturated Montmorillonite Exposed to Variably Wet Super Critical CO₂. *Environ. Sci. Technol.* **2012**, *46*, 4241−4248.

(88) Rother, G.; Ilton, E. S.; Wallacher, D.; Hauss, T.; Schaef, H. T.; Qafoku, O.; Rosso, K. M.; Felmy, A. R.; Krukowski, E. G.; Stack, A. G.; Grimm, N.; Bodnar, R. J. CO₂ Sorption to Subsingle Hydration Layer Montmorillonite Clay Studied by Excess Sorption and Neutron Diffraction Measurements. *Environ. Sci. Technol.* **2013**, *47*, 205−211.

(89) Filipponi, A.; Bowron, D. T.; Lobban, C.; Finney, J. L. Structural Determination of the Hydrophobic Hydration Shell of Kr. *Phys. Rev. Lett.* **1997**, *79*, 1293−1296.

(90) Broadbent, R. D.; Neilson, G. W. The Interatomic Structure of Argon in Water. *J. Chem. Phys.* **1994**, *100*, 7543−7547.

(91) De Jong, P. H. K.; Wilson, J. E.; Neilson, G. W.; Buckingham, A. D. Hydrophobic Hydration of Methane. *Mol. Phys.* **1997**, *91*, 99−103.

(92) Smith, S. P.; Kennedy, B. M. The Solubility of Noble Gases in Water and in NaCl Brine. *Geochim. Cosmochim. Acta* **1983**, *47*, 503−515.

(93) Vorholz, J.; Harismiadis, V. I.; Panagiotopoulos, A. Z.; Rumpf, B.; Maurer, G. Molecular Simulation of the Solubility of Carbon Dioxide in Aqueous Solutions of Sodium Chloride. *Fluid Phase Equilib.* **2004**, *226*, 237−250.

(94) Hummer, G.; Garde, S.; Garcia, A. E.; Pohorille, A.; Pratt, L. R. An Information Theory Model of Hydrophobic Interactions. *Proc. Natl. Acad. Sci. U. S. A.* **1996**, *93*, 8951−8955.

(95) Sabo, D.; Varma, S.; Martin, M. G.; Rempe, S. B. Studies of the Thermodynamic Properties of Hydrogen Gas in Bulk Water. *J. Phys. Chem. B* **2008**, *112*, 867−876.

(96) Hummer, G.; Garde, S.; Garcia, A. E.; Paulaitis, M. E.; Pratt, L. R. Hydrophobic Effects on a Molecular Scale. *J. Phys. Chem. B* **1998**, *102*, 10469−10482.

(97) Verdaguer, A.; Sacha, G. M.; Bluhm, H.; Salmeron, M. Molecular Structure of Water at Interfaces: Wetting at the Nanometer Scale. *Chem. Rev.* **2006**, *106*, 1478−1510.

(98) Bash, P. A.; Singh, U. C.; Langridge, R.; Kollman, P. A. Free Energy Calculations by Computer Simulation. *Science* **1987**, *236*, 564−568.

(99) Smith, P. E. Computer Simulation of Cosolvent Effects on Hydrophobic Hydration. *J. Phys. Chem. B* **1999**, *103*, 525−534.

(100) Paschek, D. Temperature Dependence of the Hydrophobic Hydration and Interaction of Simple Solutes: An Examination of Five Popular Water Models. *J. Chem. Phys.* **2004**, *120*, 6674−6690.

(101) Docherty, H.; Galindo, A.; Sanz, E.; Vega, C. Investigation of the Salting Out of Methane from Aqueous Electrolyte Solutions Using Computer Simulations. *J. Phys. Chem. B* **2007**, *111*, 8993−9000.

(102) Liu, M.; Besford, Q. A.; Mulvaney, T.; Gray-Weale, A. Order and Correlation Contributions to the Entropy of Hydrophobic Solvation. *J. Chem. Phys.* **2015**, *142*, 114117.

(103) Gallicchio, E.; Kubo, M. M.; Levy, R. M. Enthalpy - Entropy and Cavity Decomposition of Alkane Hydration Free Energies: Numerical Results and Implications for Theories of Hydrophobic Solvation. *J. Phys. Chem. B* **2000**, *104*, 6271−6285.

(104) Ben-Naim, A.; Egel-Thal, M. Thermodynamics of Aqueous Solutions of Noble Gases. III. Effect of Electrolytes. *J. Phys. Chem.* **1965**, *69*, 3250−3253.

(105) Barry, P. H.; Lawson, M.; Meurer, W. P.; Warr, O.; Mabry, J. C.; Byrne, D. J.; Ballentine, C. J. Noble Gases Solubility Models of Hydrocarbon Charge Mechanism in the Sleipner Vest Gas Field. *Geochim. Cosmochim. Acta* **2016**, *194*, 291−309.

(106) Torgersen, T.; Kennedy, B. M.; van Soest, M. C. Diffusive Separation of Noble Gases and Noble Gas Abundance Patterns in Sedimentary Rocks. *Earth Planet. Sci. Lett.* **2004**, *226*, 477−489.

(107) Kelley, S. Excess Argon in K−Ar and Ar−Ar Geochronology. *Chem. Geol.* **2002**, *188*, 1−22.

(108) Derkowski, A.; Szczerba, M.; Środoń, J.; Banaś, M. Radiogenic Ar Retention in Residual Silica from Acid-Treated Micas. *Geochim. Cosmochim. Acta* **2014**, *128*, 236−248.

(109) Jackson, C. R.; Parman, S. W.; Kelley, S. P.; Cooper, R. F. Noble Gas Transport into the Mantle Facilitated by High Solubility in Amphibole. *Nat. Geosci.* **2013**, *6*, 562−565.